Chapter 5

MICROFLUIDIC BIOCHIP PLATFORM FOR SERS-BASED RAPID DETECTION OF URIC ACID BIOMARKER

5.1 CHAPTER OUTLINE

In the evolving scenario of microfluidic technology, the inherent advantages attached to microfluidic technology such as low sample requirement, high precision, and controlled testing in a closed contamination-free environment has made it an ideal platform for diagnostic devices. Optical Spectroscopic techniques such as SERS in the microfluidic platform have provided a potential opportunity to develop an ultra-sensitive device for testing biomarkers. In this chapter, we have designed a microchannel comprising a passive micromixer for efficient mixing and the design was optimized using simulation (Comsol6.0). The optimized design of the device was fabricated using photolithography in SU-8 negative Photoresist. The pattern was transferred on PDMS and sealed using thermal crosslinking to get a closed contamination-free device that can mix two streams (Plasmonic Nanoparticle suspension and analyte stream) to get SERS enhancement. The device was tested for SERS enhancement using Crystal Violet dye. Promising results on crystal violet dye encouraged to testing of biomarkers obtained from the biological sample. Detection of Uric acid along with a mixture of Uric Acid and Lactic acid was done. Selectivity, Better enhancement, simple operating procedure, and contamination-free testing make this device an ideal candidate for use in the on-site detection process. The results were compared to the recently reported studies and were found to be either better or comparable to them in superior operating Conditions.

5.2 INTRODUCTION

Molecular screening of bio-fluids using optical spectroscopic techniques has distinct advantages over conventional polymerase chain reaction (PCR) and sandwich-type immunoassay techniques, as spectroscopic techniques provide highly sensitive, selective, and rapid sensing.[1-5] Spectroscopic features combined with microfluidic technologies have attracted extensive attention from researchers to develop point-of-care (POC) detection devices for preventive healthcare measurement and environment monitoring.[6,7] Among various spectroscopic techniques, Raman spectroscopy provides the most suitable detection technique for POC devices due to its high sensitivity, selectivity, label-free and non-invasive nature, and reproducibility.[8–11] Evidently, the sensitivity of Raman spectroscopy can be improved many folds (10^6 - 10^7 times) in the presence of plasmonic nanoparticles.[12] This is because the plasmonic nanoparticles create a localized electric field, which increases inelastic collision between photons and valence band electrons. In turn, the inelastic collisions significantly increase the Raman scattering, providing highly sensitive, selective, and fast detection for different analytes. The technique is known as Surface Enhanced Raman Spectroscopy (SERS).[13–16]

SERS phenomena are observed when analytes are localized in the vicinity of plasmonic nanostructures, called "hotspots".[12] While several studies have been reported encompassing hotspot engineering to increase the hotspot sites,[17,18] there are problems associated with hotspot engineering in the open substrate in terms of stability, unrepeatability, and irreproducibility.[19] To eradicate such challenges, microfluidic technologies have proven capabilities as a microfluidic platform requires very less volume of the analyte with rapid analysis, regulated flow patterns due to low Reynolds number, and amenability to realize point-of-care (POC) devices.[20] Currently, there is a

huge focus on the development of SERS-based rapid detection devices with ease of fabrication for POC diagnostics while addressing the issue of increasing the "hotspot" sites.[11] Such requirements can be met by employing microfluidic technology due to its aforementioned unique advantages.

To facilitate the maximum number of hotspot sites, mainly three different approaches have been explored in the recent past. Firstly, *in situ* growth of plasmonic nanoparticles in the microfluidic reactor and analyzing the SERS signal of the target analyte.[21–24] Tania and coworkers fabricated graphene oxide and fabricated AgNP *in situ* for Raman spectra measurement of Rhodamine 6.[25] Even though the sensitivity of Rhodamine 6 was reported as 1 nM, local thickness variation of deposited plasmonic nanoparticles poses problems for repeatability and accuracy. Secondly, stationary SERS active substrates are embedded in a microchannel and a target analyte is injected through the microchannel to capture the Raman spectra over the SERS active substrate.[26–29] This approach helped in improving the repeatability and accuracy but significantly reduces the SERS intensity.[30] Therefore, such a system requires multiple times extensive washing to be reusable or it should be disposable making the fabrication expensive and slow.

The third approach is the use of continuous flow microfluidic platforms, which utilize plasmonic nanoparticle suspension along with analyte solution flowing simultaneously in the microchannel. The SERS probe detector is placed at a point where proper mixing of the two fluid streams is obtained so that plasmonic nanoparticles and target analyte are in close vicinity.[31–34] Aggregation of the target analyte and plasmonic nanoparticle colloids is an essential condition required for hotspot formation for which proper mixing of the two fluid streams is mandatory. Such systems are easy to operate, low-cost, and amenable to real-time detection with better accuracy and efficiency.[35] However, proper mixing of the two fluid streams is a problem encountered in such systems and hinders the

repeatability of the device. To encounter this problem, appropriate mixing capabilities can be imbibed into the microchannel which is discussed in the subsequent section.

To enhance the mixing in the microfluidic device itself, various designs of the microchannel with active and passive micromixers have been explored.[36,37] Active perturbations require additional setup to provide electromagnetic, ultrasonic, or pressure perturbations, which hinders the transportability and usability of the POC device. The passive mixer uses additional variations in design like a stretch, bifurcation, split, fold, etc. which create cross-contamination, pressure variation, and phase shift while enhancing mixing in the microchannel. Various microchannel designs, such as Y-shape, T-shape, and sinusoidal-shape, to enhance mixing with phase shift in the fluid streams have been explored.[38] It was demonstrated that several factors, such as pressure perturbation, rapid bending, convergent-divergent microchannel, sharp corners in the flow path, and obstacles in the microfluidic flow path, help enhance the mixing performance in the microchannel. While the fabrication of passive mixers is complicated, the absence of an external mixing force and ease of integration into a lab-on-a-chip platform provide them a significant advantage over active micromixers.

Thus, considering the aforementioned points, in this work, a novel microfluidic-biochip consisting of a zigzag microchannel has been developed. The device was realized for enhanced mixing by introducing cornered pillars and rapid bending in microchannels to create pressure perturbations and phase shifts. Herein, the mixing obtained through the fabricated microfluidic-biochip was utilized to make a device to aggregate analyte and plasmonic nanoparticles into close vicinity, and used for SERS spectrum measurement. A complete device for rapid, POC testing was prepared to test the limit of detection, repeatability, and reproducibility of crystal violet dye and uric acid. The selectivity of the

device was tested for biological fluids lactic acid and uric acid. Analysis of device performance and its potential to be used as a POC diagnosis platform was evaluated.

5.3 MATERIALS AND METHOD

Firstly a design concept was conceived and then its simulation procedure was explained. Moving ahead with the fabrication details of the device finally testing methodology was explained.

5.3.1 Simulation Model

The simple innovative zigzag microchannel design concept and dimensions, used in the present study, are shown in Figure 5.1. The design used two inlets connected with a T-joint type reservoir. Before entering the zigzag part of the microchannel, fluid passes through a straight microchannel of 0.4 mm. Microchannel inlets have a rectangular cross-section with a width and height of 0.4 mm and 0.035 mm, respectively. Variation in design was done by varying the bending ratio of the microchannel to provide varying phase shifts in the microfluidic flow. The bending ratio of the zigzag microchannel was defined as the ratio of amplitude (A) and wavelength (λ) as shown in Figure 5.1.

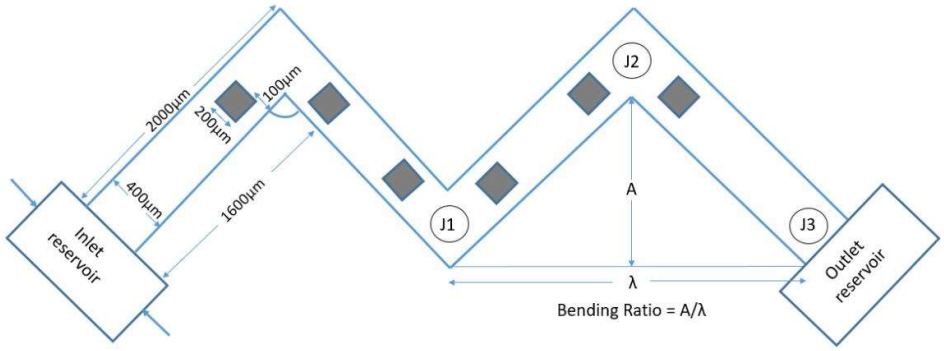

Figure 5.1 Schematic of the microchannel design for the enhanced mixing. The bending ratio is defined as the ratio of amplitude (A) and wavelength (λ) of the design as shown above.

Three different cross-section points J1, J2, and J3 at a downstream length of 3.6, 5.4, and 7.2 mm, where mixing index and Raman analysis were done, are shown in Figure 5.1. Devices with different Bending ratios (A/λ) of 0.33, 0.5, and 0.66 were named D1, D2, and D3, respectively, and analyzed at J1, J2, and J3 cross-sections of the microchannel. Gradual sorting out the most efficient design and point to obtain the optimum mixing efficacy was done.

5.3.2 Numerical Modelling

Numerical modeling of the microfluidic channel flow was carried out of single phase steady-state laminar flow of incompressible fluid and solved for Navier-Stokes equation (mass conservation) and continuity equation.[39] The mathematical expression for the two conditions is as follows.

$$\rho(u \cdot \nabla)u = \nabla \cdot [-pI + \mu(\nabla u + (\nabla u)^T)] \quad (1)$$

$$\rho \nabla \cdot (u) = 0 \quad (2)$$

Equation 1 represents the mass conservation equation where ρ represents the density of the fluid ($Kg.m^{-3}$), u is the velocity vector ($m.s^{-1}$), p is the pressure (Pa) and I is the unit vector and μ is the dynamic viscosity of the fluid ($Kg.m^{-1}.s^{-1}$). Solving these two equations provided velocity and pressure fields. Assuming there was no reaction in the mixing process convection diffusion equation was used to calculate the species concentration field as follows:

$$\nabla \cdot (-D\nabla c) + u \cdot \nabla c = 0 \quad (3)$$

Where D is the diffusion coefficient ($m^2.s^{-1}$) and c is the species concentration ($mol.m^{-3}$).

The mixing performance of the device was evaluated based on a standard deviation model as reported earlier.[40] Mixing Index (MI) based on the standard deviation of concentration was evaluated as per Equation (4).

$$\text{MI} = 1 - \frac{\sigma}{\sigma_{max}} \tag{4}$$

where σ is the standard deviation of the species concentration, and σ_{max} is the standard deviation of the unmixed state. The standard deviation of the mixed stream was calculated as per Equation (5).

$$\sigma = \sqrt{\frac{1}{N}\sum_{i=1}^{N}(C_i - C_m)^2} \tag{5}$$

where N is the number of sampling points, C_i is the mixing fraction and C_m is the optimal mixing fraction of the fluid in the microchannel. The model was implemented for water and a dye solution of the same density of 1000 $Kg.m^{-3}$ and a dynamic viscosity of 0.001 $Kgm^{-1}s^{-1}$. A diffusion coefficient of $8.5x10^{-11}$ was used for the dye solution in the water.[41] Any presence of solute was ignored for any physical property of the liquid. Also, no-slip boundary conditions and zero pressure at the outlet were considered. The effect of gravity in the z direction was ignored and thus vertical symmetry was taken into account. The inlet condition was described for the velocity and a simulation experiment was performed. Inlet concentration of 1 and 0 was used to determine the concentration field. COMSOL multiphysics (version 6.0, Comsol Inc. USA) was used for the simulation of the aforementioned model using laminar flow and transport of diluted species module. Software inbuilt physics-driven discretization was used for mesh generation, and grid independence was tested using different mesh sizes and elements. Finally, to reduce the time and computational load coarser mesh arrangements 607356, 619324, and 619350 mesh elements were used for bending ratios of 0.33, 0.5, and 0.66 respectively.

5.3.3 Materials

Silver Nitrate ($AgNo_3$), Polyvinylpyrrolidone (PVP), and Ethyl Alcohol were purchased from Sigma Aldrich, India. Sylgaurd 184 (PolyDimethylSiloxane, PDMS) with cross-linker was purchased from Dow Corning, USA. SU-8 and its developer were purchased from Microchem, USA. All other chemicals were purchased from Sigma Aldrich and used without further purification. Double-distilled deionized water was used in the preparation of samples and cleaning. Photolithography was carried out using a maskless lithography system (SF 100 from Intelligent Micropatterning LLC, St. Petersberg, FL, USA). AgNPs were characterized using a UV visible spectrophotometer (Varion 50Bio from Varion life sciences), FTIR (Perkin Elmer), and XRD instruments (Xpertpro PANalytical). TEM analysis was done by FEI Titan G2 80-300keV TEM, and Raman analysis was carried out by micro Raman STR AIRIX/Technos corporation, fitted with Princeton instruments acton spectra pro 2500i spectrometer equipped with 532nm DPSS laser (Quantum gem 50mw).

5.3.4 Fabrication of Microfluidic Biochip

A digital mask using the graphic drawing software MS paint was designed in the system, where each pixel corresponds to ~12 μm^2 on the photoresist substrate. Photoresist SU-8 2035 was coated at 3000 RPM, 100 RPM/s, and 100 RPM/s speed, acceleration, and deceleration respectively. Photoresist coating was prebaked for 12 minutes at 90°C as per the given protocol (Microchem, USA) to evaporate the solvent. The optical dose given to pattern the photoresist was at 0.98 mJ/cm^2 UV light intensity of wavelength 365 nm, for 300 seconds. After exposure, the photoresist coating with the substrate was post-baked at 90°C for 9 minutes. Finally, the sample was removed from the hot plate to cool off in the laminar airflow.

The fabricated pattern was developed using a SU-8 developer for 2 minutes. After every 30 seconds, the pattern was rinsed through Isopropyl alcohol (IPA) and then with DI water until the pattern was developed properly. Once the design pattern was developed on SU-8 photoresist, it was used as a mold to cast the pattern on the polydimethylsiloxane (PDMS). Patterned PDMS substrate was thermally bonded with another flat PDMS substrate, giving a closed microfluidic device consisting of a microchannel of the desired dimensions. The sealed pattern was punctured through a syringe needle at the inlet and outlet end and the bonding strength of the sealing was tested by flowing different flow rates of water (0.25-2 ml/min) through the microchannel for multiple samples and tested for its leakage. Samples with suitable bonding strength were then used for the SERS analysis.

5.3.5 Synthesis and Characterisation of plasmonic Nanoparticles

Single crystal nanocubes and tetrahedron Ag nanoparticles were synthesized using the standard poly-ol synthesis method.[42] To increase the yield of silver nanocubes, chloride ions were added to the solution in the form of HCl. Fabricated Ag nanoparticles were washed using isopropyl alcohol (IPA) 5 times and water 3 times. Fabricated nanoparticles were characterized using a UV visible spectrophotometer, FTIR spectroscopy, XRD, and TEM.

5.3.6 Performance Evaluation of Microfluidic Biochip using SERS

The performance of the fabricated Microfluidic-Biochip performance was evaluated by highly sensitive and selective detection of CV and UA. Fabricated microfluidic-biochip was punctured at two different points from the Inlet end and one point from the outlet end as shown in Figure 5.2. AgNPs along with the detection marker of different concentration was flown continually and simultaneously from the two inlet needles. Both

the samples were flown till the downstream exits from the outlet end. 10 minutes after flowing the two solutions, the Raman spectrum was recorded. The Raman SERS intensity was recorded by using a He-Ne laser (λ-532) at 20X objective. For each measurement reported, four different samples, with five sampling points at one junction were examined. Measurements were taken by slightly shifting the focal spot of the Raman objective at each junction, to average out the deviation in results. The testing setup of the biochip device under the Raman objective is demonstrated in Figure 5.2. Repeatability and reproducibility experiments were performed on the optimized device. To test the repeatability, the same experiment was performed multiple times for two different concentrations and the Raman intensity peak corresponding to 1618 cm^{-1} was compared and their variation in intensity was observed. The reproducibility of the device was tested on different batches of the fabricated device, and the Raman intensity peak of 1618 cm^{-1} was compared for two different concentrations of crystal violet dye.

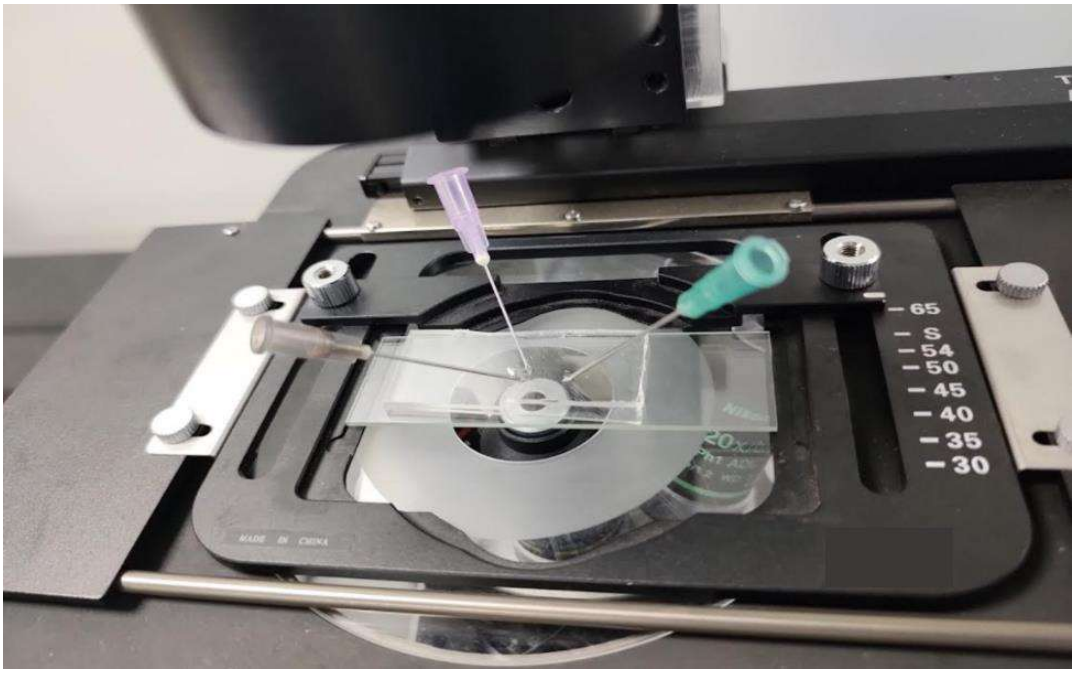

Figure 5.2 Testing setup of the device under Raman objective.

5.4 RESULT AND DISCUSSION

Firstly fabrication of the biochip is discussed with its properties along with the fabrication and characterization of nanoparticles are discussed. Mixing analysis in the device was discussed given the simulation results. Further, the SERS enhancement and device parameters were evaluated and discussed.

5.4.1 Fabrication and Characterization of Microfluidic Chip

Based on the design considerations, the microfluidic device was fabricated on the SU-8 photoresist using optical and soft photolithography as shown in Figure 5.3. In the final stage, two needles were punctured at one end, and a single needle is punctured at another end to release the pressure flow. To test the sealing strength of the biochip, the inlet, and outlet were punctured by a single needle. Sealing strength was tested by flowing different flow rates (0.25 - 2 ml/min) of water through multiple biochip devices. Biochip was found stable up to a flow rate of 1.8 ml/min. Further increasing the flow rates, a few samples were found to be detached at the outlet end.

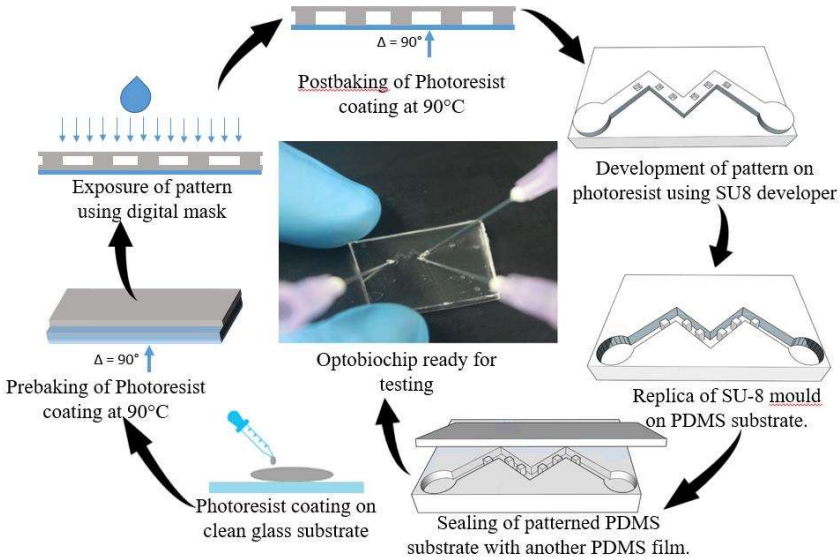

Figure 5.3 Schematic of the fabrication process of the biochip.

5.4.2 Analysis of Silver Nanoparticles (AgNp)

The as-synthesized AgNPs were subjected to different characterization techniques such as FTIR spectrum, XRD, TEM, and UV Visible absorption analysis. Figure 5.4 shows the UV Visible spectrum and FTIR analysis of synthesized AgNPs. The absorbance of the UV visible spectrum of synthesized AgNPs was recorded in the range of 200 – 1200nm. Synthesized AgNPs show absorbance in the wavelength range of 390 to 470 nm, with the highest absorbance at 441 nm wavelength, as shown in Figure 5.4a. FTIR spectrum of the fabricated AgNPs is shown in figure 5.4b. For the FTIR measurement AgNPs solution was centrifuged at 10000 RPM and the bottom concentrate was collected discarding the supernatant. The concentrate was deposited on the silicon wafer and dried powder was used for FTIR analysis. FTIR spectrum was recorded for 500 – 4500 cm^{-1} and peaks at 1312 cm^{-1} 1618 cm^{-1} and 2370 cm^{-1} were observed as shown in Figure 5.4b, which manifest the presence of AgNPs. FTIR and UV visible spectrum absorbance confirm the presence of AgNPs.

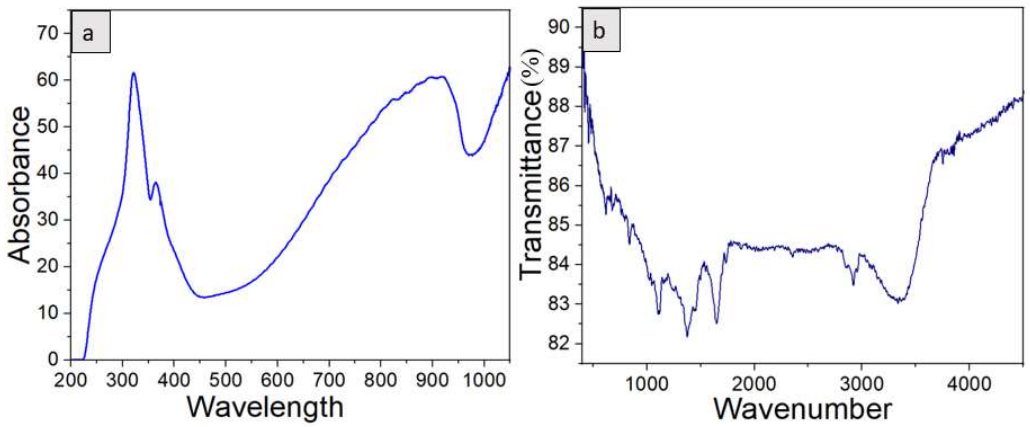

Figure 5.4 Ag nanoparticle characterization is done using a) UV Visible spectrum analysis. b) FTIR spectrum. Corresponding peaks using different techniques confirm the presence of Ag nanoparticles

Figure 5.5a shows XRD analysis peaks of the AgNPs. XRD analysis is done using a Cu-Kα radiation source in a scattering range of 5-95° on the instrument operating at a voltage of 45 kV and a current of 40 mA. It can be seen from Figure 5.5a that 2θ peaks at 37.9°, 44.4°, 64.6°, 76.9° and 81.59 ° representing hkl planes at (111) (200) (220) (311) and (004) confirms the presence of AgNPs. The XRD diffraction data was found consistent with the JCPDS data (file no. 89-3722), which denotes the face-centered cubic (FCC) structure of Ag with a = b = c = 4.111 A°. XRD patterns reflect the presence of AgNPs, and the size of fabricated nanoparticles is calculated to be ~68 nm. An additional peak at 2θ = 32° is also observed, which is corresponding to the oxidized silver nanoparticles (AgO).[42] Figure 5.5b shows the TEM Images of the synthesized AgNPs. TEM images show the size and shape of synthesized nanoparticles. The Inset image in Figure 5.5b shows the cubic shape of the synthesized AgNPs. The average size of the nanoparticles was measured to be 68 nm after analyzing the images through Image J.

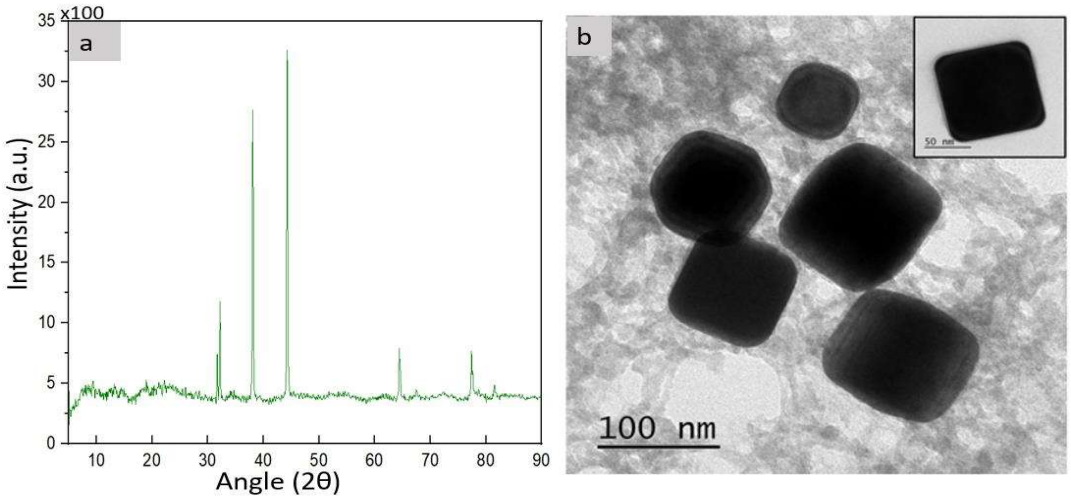

Figure 5.5 a) XRD spectrum and b) TEM images of synthesized AgNPs nanoparticle.

5.4.3 Mixing Analysis

When there is bending in a microchannel, pressure, and velocity gradients are created on the fluid towards the outer wall due to centrifugal forces. These pressure and velocity gradients create secondary vortex formation which increases with an increase in Dean number defined as

$$\text{Dean number K} = \sqrt{\frac{Dh}{2r}}Re$$

Rapid bending in the microchannel increases the hydraulic diameter of the flow at the corners and the introduction of pillars inside the microchannel creates pressure perturbation which increases vortex formation. This vortex formation at each bending junction helps in improving the mixing performance of the device. Figure 5.6 shows streamlined plots at different lengths across the microchannel and for different bending ratios of the microchannel of the biochip, to explain the effect of secondary flows, bending, and the presence of pillars. Streamline plots show that there is no vortex formation and the fluid stream path shows negligible crossing at the start. Increasing length downstream provides significant streamline crossing and vortex formation, especially after the appearance of pillars in the microchannel which increases the mixing performance of the device. Figure 5.6 shows that while increasing the bending ratio (A/λ), the streamline crossover increases, and mixing performance is improved.

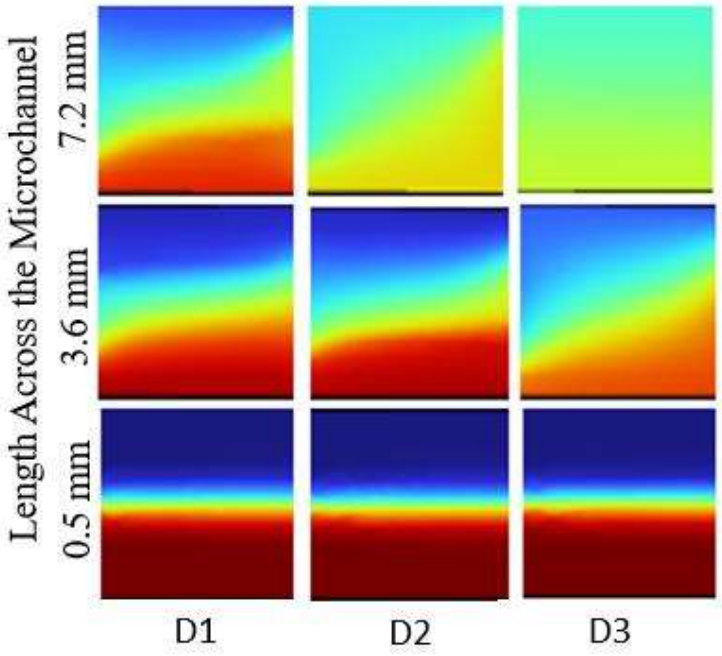

Figure 5.6 Concentration contour plot in the biochip microchannel varying in its bending ratio at different lengths downstream.

Different values of mixing index were calculated at the outlet reservoir for the three samples D1, D2, and D3 were plotted. With increasing bending ratio streamlined contour at the outlet, the reservoir was found to be more intermingled, and hence mixing is expected to be more efficient with increasing bending ratio. The mixing index calculated at the outlet cross-section of the three devices also confirms this finding as shown in Figure 5.7a. Device D3 with the highest bending ratio of 0.66 provided the most efficient mixing. Device D3 was then subjected to test the mixing across its downstream length. At increasing length towards the downstream at each bending junction, vortex formation occurred and hence mixing was enhanced. At the cross-section of each junction of device D3, the mixing index was calculated. Figure 5.7b shows the mixing index calculated at different junctions of the device D3 We found that with the increasing length towards the downstream of the microchannel, the mixing index was increased at each junction.

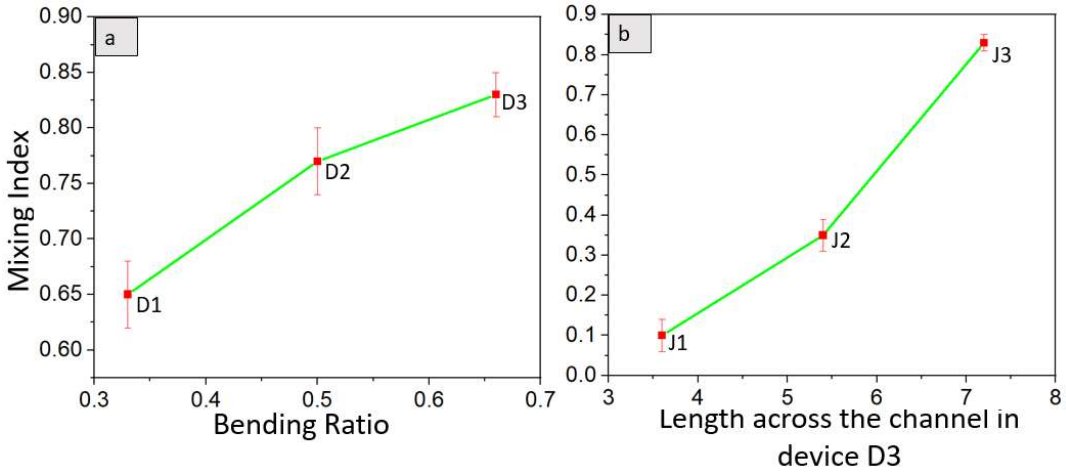

Figure 5.7 Mixing Index at (a) junction J3 in the three different devices varying in its bending ratio and (b) mixing index at the different junctions of the biochip microfluidic channel.

The aforementioned analysis confirms that mixing in a microfluidic device is sufficient enough to bring plasmonic nanoparticles and target analyte into close contact. The further microfluidic-fluidic device was tested for the SERS enhancement activity and a proof of concept was demonstrated that such microfluidic biochip devices can be used for a portable SERS-based POC device. A conducive result in the SERS activity will also provide experimental validation of the simulation results.

5.4.4 Experimental Validation of Fabricated Device by SERS analysis of the Crystal Violet Dye

Mixing of the fluid streams in the microfluidic-biochip laid the ground for the possibility of Raman spectrum analysis in the device. In the earlier sections, it was demonstrated that with increasing bending ratio and increasing length, the mixing index increases. Thus, the variation in these two parameters was investigated for the Raman spectrum measurement. When a target analyte-molecule of crystal violet dye and silver nanoparticles were flown simultaneously, the two fluid streams mixed with an increase

in length of the microchannel, and hence an enhanced Raman spectrum peak was observed. A crystal violet solution of 10^{-6} M along with aqueous silver (Ag) nanoparticle suspension was flown in three different device configurations, and the Raman spectrum using 20X objective, was measured at the junction J3 of downstream length 7.2 mm. The device giving maximum enhancement in Raman intensity was considered to provide the most exhaustive mixing. Further, the impact of length was evaluated. In the optimum bending ratio (A/ λ ratio) design of the microfluidic-biochip, a similar experiment was performed and Raman intensity was measured at different lengths of the microchannel. The junction point was supposed to facilitate the most enhanced mixing, where enhancement in the Raman intensity peak of crystal violet is maximum. The Raman analysis was performed at different cross-sections J1, J2, and J3 at lengths 3.6, 5.4, and 7.2mm towards the downstream.

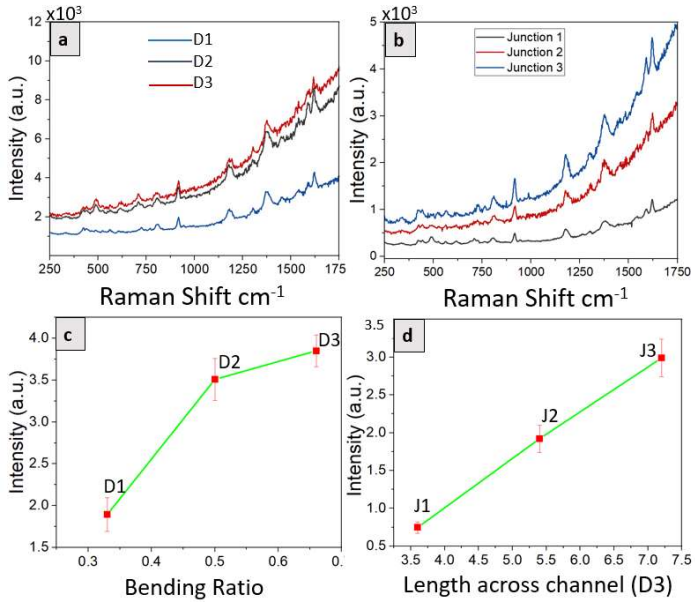

Figure 5.8 Raman spectrum of Crystal violet dye for three devices with a) different bending ratios of microchannels. b) different junctions of the microchannels. c) Bending ratio vs intensity plot for the peak of 1390 cm^{-1}. d) Length across microchannel vs intensity plot for the peak of 1390 cm^{-1}.

5.4.5 Effect of Microchannel Bending

In the proposed device design, mixing enhancement mainly relies upon the sharp bending/turn of the microchannel, consequently increasing phase shift and hence better mixing. Figure 5.8a shows the crystal violet peaks observed when Ag nanoparticle and crystal violet dye of 10^{-6} M concentration was flown in the three devices D1, D2, and D3 at bending ratios (A/λ) of 0.33, 0.5, and 0.66. Signature Raman spectrum peaks of crystal violet at 935 Cm^{-1} (ring skeletal vibration), 1175 Cm^{-1} (C-H in-plane bending), 1390 Cm^{-1} (N phenyl stretching), 1620 Cm^{-1} (C-C stretching) are evident and short peaks at 1535 Cm^{-1} and 1591 Cm^{-1} are also visible (representing C-C stretching)[43]. These peaks confirm that mixing in the device is sufficient to bring analyte and plasmonic nanoparticles in the close vicinity and detect the crystal violet dye. As the bending ratio (A/λ) of the microfluidic channel in the biochip is increased, phase shift and hence mixing increases. It can be observed from Figures 5.8a and 5.8c that device D3 with a bending ratio (A/λ) of 0.66 provides the most intense peaks, suggesting that the mixing of analyte and plasmonic nanoparticles, in this case, must have been most efficient.

5.4.6 Effect of Increasing Length of Mixing in the Device

It is imperative to know the mixing at different lengths downstream of the device. Thus, the device D3 with a bending ratio of 0.66 was subjected to similar experimental conditions as above and the Raman spectrum was measured at different junctions (J1, J2, and J3) at the increasing length of 3.6 mm, 5.4 mm, and 7.2 mm and a comparison of Raman intensity peak of crystal violet was observed. Figure 5.8b shows the Raman intensity of crystal violet at the increasing length of the microchannel in the biochip device. It is evident that with increasing length, all the signature peaks of crystal violet are visible, suggesting that the mixing of the two fluid streams (analyte and AgNp)

increases with increasing length. The corresponding junctions J1, J2, and J3 at increasing lengths are indicated in Figure 5.1. It was observed that the enhancement in the Raman intensity was maximum in device D3 at junction J3 (7.2mm downstream length). Therefore, all the further experiments were performed using these optimized device parameters.

5.4.7 SERS Performance Evaluation of Microfluidic Biochip Device with Biomarker Sensing

The fabricated device was validated by testing the sensing limit by flowing aqueous plasmonic nanoparticle suspension and different synthetic and biological markers. Crystal violet dye, uric acid, and of different concentrations ranging from 10^{-3} M to 10^{-15} M along with Ag nanoparticles were used for the analysis. Raman spectra of all the analytes in device D3 at junction J3 (7.2 mm length in the microchannel) were recorded. Figure 5.9a shows that peaks corresponding to crystal violet at 935 cm^{-1}, 1175 cm^{-1}, 1390 cm^{-1}, 1620 cm^{-1}, 1535 $cm^{-1,}$ and 1591 cm^{-1} are evident for the 10^{-3} and 10^{-6} M concentrations. However, as the concentration decreases, some of the peaks at 1535 Cm^{-1} and 1621 Cm^{-1} get diminished. For the crystal violet concentration of 10^{-12} M, peaks at 935 Cm^{-1}, 1175 Cm^{-1}, 1390 Cm^{-1}, and 1590 Cm^{-1} are visible. For lower concentrations of crystal violet, it was found that the peaks get merged and their detection becomes difficult. Thus, the fabricated device was found to be effective for a picomolar level of detection of 10^{-12} M aqueous crystal violet dye solution.

The performance of the chip was evaluated in terms of relative standard deviation (RSD) enhancement factor (EF), limit of detection (LoD), uniformity, reproducibility, and stability. RSD values were calculated for four different samples, at five different spots on each sample. For crystal violet (1390cm^{-1}), the RSD value was calculated to be

2.7%. RSD values show a fair reproducibility of the device for crystal violet dye. The enhancement factor (EF) in the fabricated device for Crystal violet dye, was calculated to be $2x10^7$ by the formula $EF = (I_{SERS}/I_s) X (C_s/C_{SERS})$. The limit of detection was calculated by the relation $LOD = 3\sigma/d$ and found to be $8.9x10^{-11}$ for crystal violet dye.

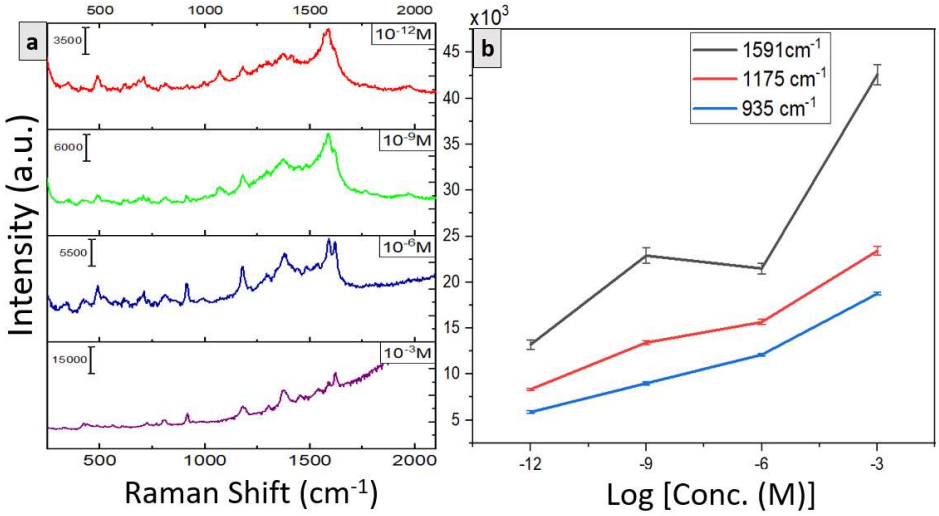

Figure 5.9 SERS activity of crystal violet dye in the fabricated device (a) Sensitivity plot (b) Concentration vs. intensity plot.

Motivated by the significant SERS enhancement in the results, the fabricated device was tested for the SERS spectra of Uric acid (UA) of different concentrations (10^{-3}- 10^{-9}). UA along with AgNps was flown in the device and Raman intensity values have been measured. Results depicted in Figure 5.10a shows that peaks corresponding to UA at 624 cm^{-1} (skeletal ring deformation vibration), 800 cm^{-1} (C-H bond stretching), 1260 Cm^{-1} (C-N stretching vibration) and 1400 Cm^{-1} (C-H bending) indicate the presence of the uric acid in the sample.[44] However, peaks in the range of 950 – 1150 cm^{-1} are not obtained in the sample, which may be because in the SERS spectrum of the UA, spectral band positions differ considerably from the conventional Raman spectrum which makes it

difficult to trace UA in biological fluids through SERS mechanism.[45,46] Level of detection of Uric acid was found to be $50x10^{-9}$M, however, at such concentration, SERS peaks for Uric acid were dissolved in the noise as shown in figure 5.10a.

Enhancement factor, LoD, and RSD values of uric acid were calculated and found to be $3.1x10^{3}$, $3.2x10^{-7,}$ and 2.9% respectively. Results show that the device is producing uniform results with a very small variation.

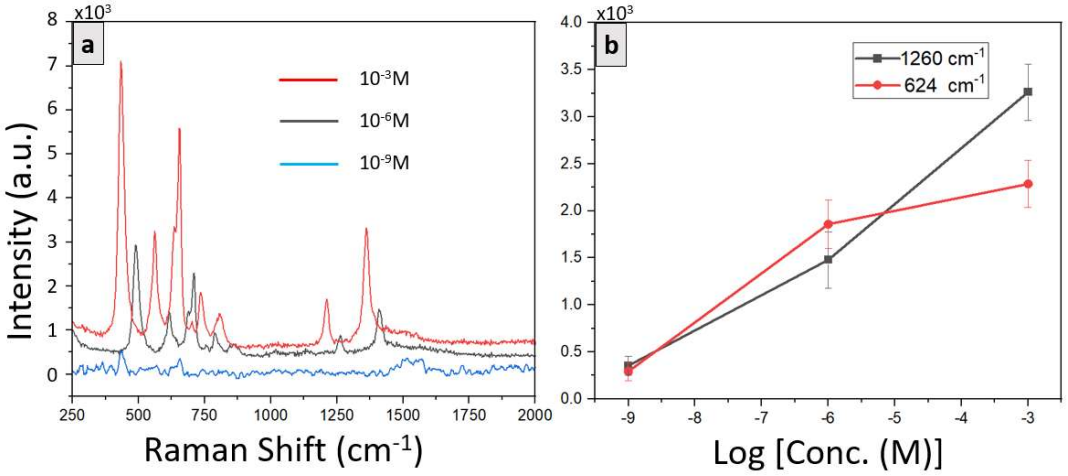

Figure 5.10 SERS spectra UA in the fabricated device (a) Sensitivity plot (b) Concentration vs Intensity plot.

5.4.8 Selectivity of the Microfluidic Chip

Selectivity was tested for a mixture of uric acid and lactic acid. Plasmonic nanoparticle suspension along with a mixture of uric acid and lactic acid in different concentrations was flown and SERSspectrum was recorded and analyzed for the peaks of both the components. Figure 5.11 shows that peaks at 624 cm^{-1}, 1400 $cm^{-1,}$ and diminished peaks at 800 cm^{-1} and 1035 cm^{-1} corresponding to uric acid are identifiable. Characteristic peaks corresponding to lactic acid are also clearly visible at 1285 cm^{-1} and 1400 cm^{-1} which demonstrates the better selectivity of the device. The characteristic peak

of 1400 cm^{-1} of lactic acid and uric acid seems to be merged, which is not identifiable separately. Peaks of lactic acid will be observed more predominantly at 632 nm laser excitation.

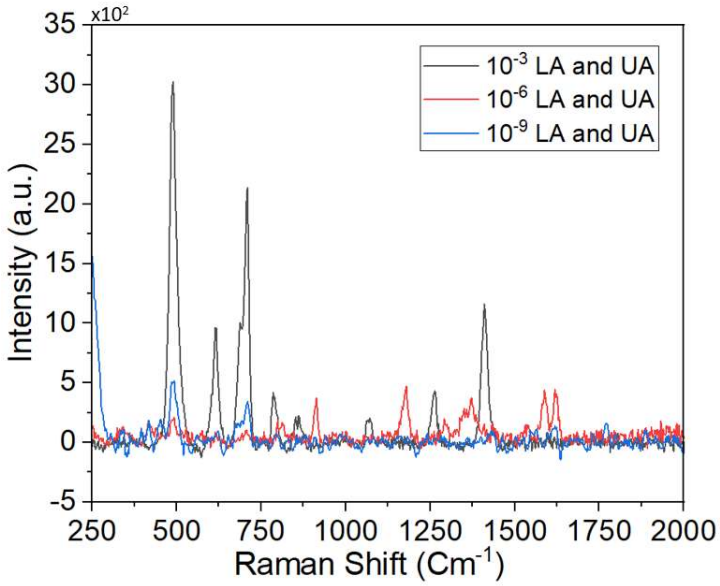

Figure 5.11 Selectivity of the device for a mixture of uric acid and lactic acid.

5.4.9 Performance Evaluation of Microfluidic Chip

Uniformity and reproducibility of the biochip are tested experimentally and are demonstrated in Figure 5.12 a and b. To test the repeatability, Crystal violet dye (10^{-3}M and 10^{-6}M) with Ag nanoparticles suspension flowed in the microfluidic bio-chip device and a relative comparison of the peak corresponding to 1620 cm^{-1} was compared in Figure 5.12a. It can be seen that for multiple experiments, results are consistent with small variations. Intensity variation between different samples may originate due to the variation of droplet residue or mixing of the two fluid streams. The reproducibility of the device is tested by performing the same experiment as above with 10^{-6} M concentration of crystal violet and Ag nanoparticles (AgNPs) suspension on different batches of D3 biochip. Results shown in Figure 12b demonstrate that even being tested on different

batches, we can differentiate between small concentration variations and provide repeatable and reproducible results. Since these results are marker-independent, similar results are expected for other biomarkers. The device was tested after consecutive months for similar testing and results were consistent with the previous results, hence stability was not found to be a significant concern in this case.

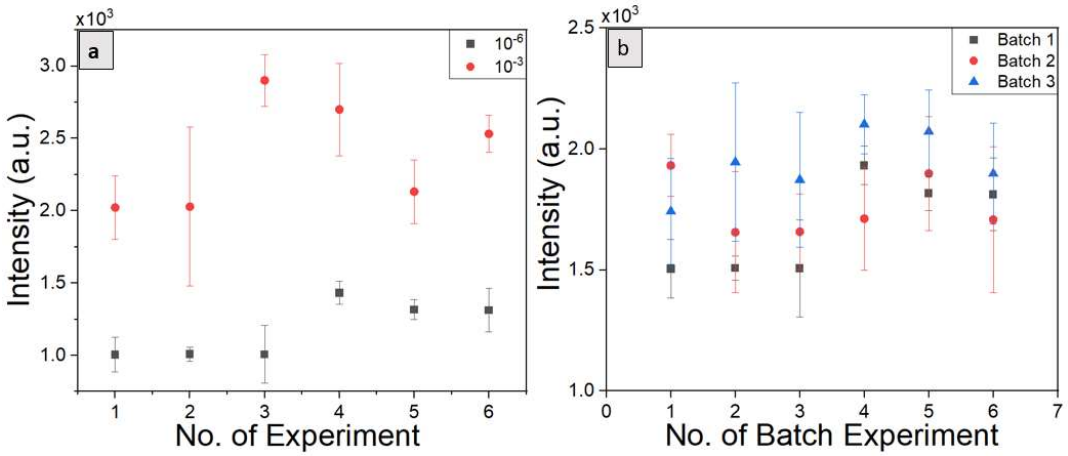

Figure 5.12 Repeatability and reproducibility experiment. a) Single device is used to detect the two different concentrations by multiple operators and peak intensity corresponding to 1618 cm^{-1} peak was compared. b) Three different batches of the optimized device were used to detect the same concentration of crystal violet dye. Results show that the D3 device is consistently reproducible and repeatable under practical limitations.

Device performance and limit of detection (LoD) study was performed using a 20X objective of the Raman spectroscope. Further, enhancement in the results can be obtained by using the 50X objective, however, the 50X objective will lead to a low working distance and in turn requires a very thin layer of PDMS to seal the device which may pose problems due to the large flexibility of the sealing layer.

The fabricated device was found to be effectively sensitive, selective, repeatable, and reproducible for synthetic dyes and biological markers. The mixing performance and sensor parameters of the fabricated device for different markers are summarized in Table 5.1

Table 5.1 Mixing and sensing parameters of the fabricated device.

Device name (A/λ)	Mixing Index (MI)		
	J1 (3.6mm)	J2 (5.4mm)	J3 (7.2mm)
D1 (0.33)	0.1	0.28	0.64
D2 (0.5)	0.1	0.31	0.76
D3 (0.66)	0.1	0.35	**0.83**
Performance evaluation of the D3 device			
Marker	Parameters		
	LoD	EF	Uniformity (%RSD)
CV	8.9×10^{-11}	2×10^{7}	2.7%
UA	3.2×10^{-7}	3.2×10^{3}	2.9%

A comparison of earlier reported techniques for the detection of similar markers, and different techniques of plasmonic nanoparticles, decorated in the microfluidic channel are summarized in Table 5.2.

Table 5.2 Different techniques are used for the detection of crystal violet, and microfluidic devices are used for continuous flow detection mechanisms.

Sr. no.	Technique used	Analyte detected	Efficacy/LoD	Reference
1	Ag nanoparticles reduced onto the porous silicon surface	Crystal Violet	$1x10^{-10}$ M	15
2	Ag and Cu particles decorated on Cicada wing	Crystal Violet	$1x10^{-11}$ M	16
3	Hexagonal boron nitride and Au nanocomposites	Crystal violet	$1x10^{-15}$ M	47
4	Ag nanoparticles loaded on paper substrate	Crystal violet	$1x10^{-12}$	48
5	Ag nanoparticles and carbon dots with peroxidase	Uric acid	$16.8x10^{-9}$	49
6	Au nanoparticle decorated paper substrate	Uric acid	$1.1x10^{-8}$	50
7	Electrochemical sensing method using RGO	Uric acid	$8.8x10^{-6}$	51
8	Ag NP suspension flowed along with the analyte in the device fabricated	Crystal violet and Uric acid	$1x10^{-12}$M for CV, $50x10^{-9}$ M for UA	Present work

The present work illustrates the efficacy of the micromixer-embedded microfluidic biochip device, for the detection of UA biomarkers. The detection limit of the device is well below the critical limit, and the extension of the work for the real samples can provide a point-of-care detection platform for onsite detection.

5.4.10 Experimental Observation and Future Scope

Above mentioned results shows that the fabricated device is capable of providing enhanced mixing and provides a significantly enhanced Raman signal than the previously reported techniques for crystal violet dye. The repeatability and reproducibility of the device are also under the control limit. The intended application of the device is to be used as a point of care diagnosis equipment, thus, the fabricated microfluidic-biochip is examined on a lower magnification objective of 20X magnification instead of a 50X objective. Interestingly, the stability of the substrate, in this case, is not an issue, as the plasmonic nanoparticles and analyte molecules are brought into close vicinity exactly at the time of detection. Working at lower magnification is more likely to be useful in point-of-care diagnosis equipment. Uric acid concentration of more than 4.5µm concentration in the male body and 3.5µm in the female body is the upper limit. Our detection limit is well below this level and thus the device can be considered useful in practical applications. Further, this setup will be a spectrometer to use this setup as point-of-care diagnosis equipment.

5.5 CONCLUSION

Herein, a microfluidic-biochip for point-of-care device application using SERS as a read-out was developed and tested. Novelty in the microchannel design of the biochip was introduced using rapid bending along with cornered pillars just before bending in the microchannel. The design of the microchannel also acted as contraction and expansion at the corner points. The chip was fabricated by using simple one-step maskless lithography and then subsequently replicated on the PDMS using soft-lithography. Further, the device was bonded using thermal sealing and tested for leakage by flowing water at a flow rate of less than 1.8 ml/min and no leakage was found. Thereafter, the device was subjected

to the analysis of CV a dye under continuous flow conditions along with silver nanoparticles (AgNPs). The optimized device design configuration for Raman analysis was found to be D3 at the downstream length of 7.2mm. Mixing was also demonstrated to be enhanced along with the downstream of the device. Results were in line with the simulation results and it was found that increasing the bending ratio (A/λ) of the zigzag microchannel in the device, gave better mixing between silver nanoparticles and the target analyte. The limit of detection of the device for crystal violet dye, uric acid was found to be 8.9×10^{-11} M and 3.2×10^{-8} M with a 20X objective. The device was demonstrated to be selective towards a mixture of lactic acid and uric acid biomarkers and was reproducible and repeatable. Working at a lower magnification of the Raman spectrophotometer allows the device to be used in a robust and portable setup. The fabricated device shows potential features to be developed as point-of-care diagnosis equipment.

5.6 REFERENCES

[1]. Kitane, D. L.; Loukman, S.; Marchoudi, N.; Galiana, A. F.; Zahra, F.; Ansari, E.; Jouali, F.; Badir, J.; Gala, J. L.; Bertsimas, D. A Simple and Fast Spectroscopy - Based Technique for Covid - 19 Diagnosis. Sci. Rep. 2021, 1–11.

[2]. Ishikawa, J.; Maeshima, A.; Mellinger, A.; Dur, A.; Bourbon, M. Two-Dimensional Polyacrylamide Gel Electrophoresis for Metalloprotein Analysis Based on Differential Chemical Structure Recognition by CBB Dye. Sci. Rep. 2019, 9(1), 1–9.

[3]. Tang, J.; Chen, W.; Ju, H. Rapid Detection of Pesticide Residues Using a Silver Nanoparticles Coated Glass Bead as Nonplanar Substrate for SERS Sensing. Sens. Actuators B. 2019, 287, 576-583

[4]. Niu, S.; Qu, L.; Zhang, Q.; Lin, J. Fluorescence Detection of Thrombin Using Autocatalytic Strand Displacement Cycle Reaction and a Dual-Aptamer DNA Sandwich Assay. Anal. Biochem. 2012, 241, 362–367.

[5]. Agents, F.; Nawrot, W. A. Fluorescent Biosensors for Detection Vital Body. Sensors. 2018, 18, 2357.

[6]. Con, L. R.; Black, G. P.; Wilson, B. C.; Lowe, D. J.; Theakstone, A. G. Vibrational Spectroscopic analysis of Blood for Diagnosis of Infections and Sepsis : A Review of Requirement for a Rapid Diagnostic Test. Anal. Methods. 2021, 13, 157–168.

[7]. Graham, S. A.; Segal, E. Lab-on-a-Chip Devices for Point-of-Care Medical Diagnostics, Advances in Biochemical Engineering/Biotechnology. 2020, 179, 247-265.

[8]. Xu K.; Zhou, R.; Takei, K.; Hong, M. Toward Flexible Surface-Enhanced Raman Scattering (SERS) Sensors for Point-of-Care Diagnostics. Advance Science. 2019, 6, 1900925.

[9]. Wang, L.; Wang, X.; Cheng, L.; Ding, S.; Wang, G.; Choo, J.; Chen, L. Biosensors and Bioelectronics SERS-Based Test Strips : Principles , Designs and Applications. Biosens. Bioelectron. 2021, 189, 113360.

[10]. Jahn, I. J.; Weber, K.; Bocklitz, T. W.; Popp J. Surface-Enhanced Raman Spectroscopy and Micro Fluidic Platforms: Challenges, Solutions and Potential Applications. Analyst. 2017, 142, 1022–1047.

[11]. Marks, H.; Schechinger, M.; Garza, J.; Locke, A.; Coté, G. Surface Enhanced Raman Spectroscopy (SERS) for in Vitro Diagnostic Testing at the Point of Care. Nanophotonics. 2017, 6, 681–701.

[12]. Kahraman, M.; Mullen, E. R.; Korkmaz, A.; Wachsmann-Hogiu, S. Fundamentals and Applications of SERS-Based Bioanalytical Sensing. Nanophotonics. 2017, 6, 831–852.

[13]. Kannan, P. K.; Shankar, P.; Blackman, C. Recent Advances in 2D Inorganic Nanomaterials for SERS Sensing. Adv. Mater. 2019, 31(34), 1–27.

[14]. Lee, H. K.; Lee, H.; Lin, S.; Phan-quang, G. C.; Han, X.; Lay, L.; Fan, Y. Designing Surface-Enhanced Raman Scattering (SERS) Platforms beyond Hotspot Engineering : Emerging Opportunities in Analyte Manipulations and Hybrid Materials. Chem. Soc. Rev. 2019, 48, 731–756.

[15]. Harraz, F. A.; Ismail, A. A.; Bouzid, H.; Al-sayari, S. A.; Al-hajry, A.; Al-assiri, M. S. Surface-Enhanced Raman Scattering (SERS) -Active Substrates from Silver Plated-Porous Silicon for Detection of Crystal Violet. Appl. Surf. Sci. 2015, 331, 241–247.

[16]. Yan, X.; Wang, M.; Sun, X.; Wang, Y.; Shi, G.; Ma, W.; Hou, P. Sandwich-like Ag@Cu@CW SERS Substrate with Tunable Nanogaps and Component Based on the Plasmonic Nanonodule Structures for Sensitive Detection Crystal Violet and 4-Aminothiophenol. Appl. Surf. Sci. 2019, 479, 879–886.

[17]. Sanci, R.; Volkan, M. Surface-Enhanced Raman Scattering (SERS) Studies on Silver Nanorod Substrates. Sensors Actuators, B Chem. 2009, 139, 150–155.

[18]. Zhang, C.; Li, C.; Yu, J.; Jiang, S.; Xu, S.; Yang, C.; Liu, Y. J.; Gao, X.; Liu, A.; Man, B. SERS Activated Platform with Three-Dimensional Hot Spots and Tunable Nanometer Gap. Sensors Actuators, B Chem. 2018, 258, 163–171.

[19]. Chen, N.; Xiao, T.; Luo, Z.; Kitahama, Y.; Hiramatsu, K.; Kishimoto, N.; Itoh, T.; Cheng, Z.; Goda, K. Porus Carbon Nanowire Array for Surface-Enhanced Raman Spectroscopy. Nat. Commun. 2020, 11, 1–8.

[20]. Sachdeva, S.; Davis, R. W.; Saha, A. K. Microfluidic Point-of-Care Testing: Commercial Landscape and Future Directions. Front. Bioeng. Biotechnol. 2021, 8, 1–14.

[21]. Bernatova, S.; Donato, M. G.; Jez, J.; Magazzu, A.; Marago, O. M.; Zema, P. Wavelength-Dependent Optical Force Aggregation of Gold Nanorods for SERS in a Microfluidic chip. J. Phys. Chem. C 2019, 123, 5608-5615.

[22]. Lafuente, M.; Pellejero, I.; Clemente, A.; Urbiztondo, M. A.; Mallada, R.; Reinoso, S.; Pina, M.P.; Gandia, L. M. In Situ Synthesis of SERS Active Au@POM Nanostructures in a Microfluidic Device for Real Time Detection of Water Pollutants. ACS Appl. Mater Interfaces. 2020, 12, 36458-36467.

[23]. Lee, M. R.; Lee, H. K.; Yang, Y.; Koh, C.S.L.; Lay, C. L.; Lee, Y. H.; Phang, I. Y.; Ling, X. Y. Direct Metal Writing and Precise Positioning of Gold Nanoparticles within Microfluidic Channels for SERS Sensing of Gaseous Analytes. 2017, 45, 39584–39593.

[24]. Nie, Y.; Jin, C.; Zhang, J. X. J. Microfluidic In Situ Patterning of Silver Nanoparticles for Surface-Enhanced Raman Spectroscopic Sensing of Biomolecules. ACS Sensors. 2021, 6, 2584-2592.

[25]. Naqvi, T. K.; Srivastava, A. K.; Kulkarni, M. M.; Siddiqui, A. M. Silver Nanoparticles Decorated Reduced Graphene Oxide (RGO) SERS Sensor for Multiple Analytes. Appl. Surf. Sci. 2019, 478, 887–895.

[26]. Yang, K.; Zong, S.; Zhang, Y.; Qian, Z.; Liu, Y.; Zhu, K.; Li, L.; Li, N.; Wang, Z.; Cui, Y. Array-Assisted SERS Microfluidic Chips for Highly Sensitive and Multiplex Gas Sensing. ACS Appl. Mater Interfaces. 2020, 12, 1395-1405.

[27]. Bai, S.; Serien, D.; Hu, A.; Sugioka, K. 3D Microfluidic Surface-Enhanced Raman Spectroscopy (SERS) Chips Fabricated by All-Femtosecond-Laser-Processing for Real-Time Sensing of Toxic Substances. Adv. Funct. Mater. 2018, 28, 1–10.

[28]. Kim, D.; Campos, A. R.; Datt, A.; Gao, Z.; Rycenga, M.; Burrows, N. D.; Greeneltch, N. G.; Mirkin, C. A.; Murphy, C. J.; Van, D. R. P.; Haynes, C. L. Microfluidic-SERS Device for One-Shot Limit-of-Detection. Analyst. 2014, 139, 3227–3234.

[29]. Guo, J.; Zeng, F.; Guo, J.; Ma, X. Preparation and Application of Microfluidic SERS Substrate : Challenges and Future Perspectives. J. Mater. Sci. Technol. 2020, 37, 96–103.

[30]. Mao, H.; Wu, W.; She, D.; Sun, G.; Lv, P.; Xu, J. Microfluidic Surface-Enhanced Raman Scattering Sensors Based on Nanopillar Forests Realized by an Oxygen-Plasma-Stripping-of-Photoresist Technique. Small. 2013, 10, 127–134.

[31]. Lu, J. and Shih, W. Microfluidic Surface-Enhanced Raman Scattering Sensor with Monolithically Integrated Nanoporous Gold Disk Arrays for Rapid and Label-Free Biomolecular Detection. J. of Biomedical Optics. 2014, 19, 111611.

[32]. Wang, Z.; Ye, S.; Zhang, N.; Liu, X.; Wang, M. Triggerable Mutually Amplified Signal Probe Based SERS- Microfluidic Platform for the Effecient Enrichment and Quantitative Detection of MiRNA. Anal. Chem. 2019, 91, 5043-5050.

[33]. Wang, C.; Yu, C. Analytical Characterization Using Surface-Enhanced Raman Scattering (SERS) and Microfluidic Sampling. Nanotech. 2015, 26, 092001.

[34]. Su, W.; Gao, X.; Jiang, L.; Qin, J. Microfluidic Platform towards Point-of-Care Diagnostics in Infectious. J. Chromatogr. A. 2015, 1377, 13–26.

[35]. Pu, H.; Xiao, W.; Sun, D. SERS-Microfluidic Systems : A Potential Platform for Rapid Analysis of Food Contaminants. Trends in Food Science and Technology. 2017, 70, 114–126.

[36]. Yang, R. and Tai, C. Micromixer Utilizing Electrokinetic Instability-Induced Shedding Effect. Electrophoresis. 2006, 27, 4982-4990.

[37]. Ward, K. and Fan, Z. H. Mixing in Microfluidic Devices and Enhancement Methods. J. Micromech. Microeng. 2015, 25, 094001.

[38]. Lee, C.; Chang, C.; Wang, Y.; Fu, L. Microfluidic Mixing : A Review. J. Mol. Science. 2011, 12, 3263–3287.

[39]. Gidde, R. R.; Pawar, P. M.; Ronge, B. P.; Misal, N. D.; Kapurkar, R. B.; Parkhe, A. K. Evaluation of the Mixing Performance in a Planar Passive Micromixer with Circular and Square Mixing Chambers. Microsyst. Technol. 2018, 24, 2599–2610.

[40]. Hashmi, A. and Xu, J. On the Quantification of Mixing in Microfluidics. J. Lab. Autom. 2014, 19, 488–491.

[41]. Pioro, I. L. and Duffey, R. B. Experimental Heat Transfer in Supercritical Water Flowing inside Channels (Survey). Nucl. Eng. Des. 2005, 235, 2407–2430.

[42]. Han, H. J.; Yu, T.; Woo-sik, K.; Im, S. H. Highly Reproducible Polyol synthesis for silver nanocubes. J. Crys. Growth. 2017, 469, 48-53.

[43]. Mao, A.; Jin, X.; Gu, X.; Wei, X.; Yang, G.; Rapid, Green Synthesis and Surface-Enhanced Raman Scattering Effect of Single-Crystal Silver Nanocubes Rapid , Green Synthesis and Surface-Enhanced Raman Scattering Effect of Single-Crystal Silver Nanocubes. J. Mol. Struct. 2012, 1021, 158–161.

[44]. Huang, C. and Hsiao, H. C. Nanostructured EC-SERS Active Working Electrode for Rapid Detection of Uric Acid. Sensors. 2020, 20, 7066.

[45]. Goodall, B. L.; Robinson, A. M.; Brosseau, C. L. Electrochemical-Surface Enhanced Raman Spectroscopy (E-SERS) of Uric Acid: A Potential Rapid Diagnostic Method for Early Preeclampsia Detection. Phys. Chem. Chem. Phys. 2013, 15, 1382–1388.

[46]. Pucetaite, M.; Velicka, M.; Pilipavicius, J.; Beganskiene, A.; Ceponkus, J.; Sablinskas, V. Uric Acid Detection by Means of SERS Spectroscopy on Dried Ag Colloidal Drops. J. Raman Spectrosc. 2016, 47, 681–686.

[47]. Zhang, H.; Li, G.; Li, S.; Xu, L.; Tian, Y.; Jiao, A.; Liu, X.; Chen, F.; Chen, M. Boron Nitride / Gold Nanocomposites for Crystal Violet and Creatinine Detection by Surface-Enhanced Raman Spectroscopy. Appl. Surf. Sci. 2018, 457, 684–694.

[48]. Verma, M.; Naqvi, T. K.; Tripathi, S. K.; Kulkarni, M. M.; Dwivedi, P. K. Paper Based Low-Cost Flexible SERS Sensor for Food Adulterant Detection. Environ. Technol. Innov. 2021, 24, 102033.

[49]. Wang, A.; Guan, C.; Shan, G.; Chen, Y.; Wang, C.; Liu, Y. A Nanocomposite Prepared from Silver Nanoparticles and Carbon Dots with Peroxidase Mimicking Activity for Colorimetric and SERS-Based Determination of Uric Acid. Microchim. Acta. 2019, 186, 644.

[50]. Naqvi, T. K.; Bajpai, A.; Bharati, M. S. S.; Kulkarni, M. M.; Siddiqui, A. M.; Soma, V. R.; Dwivedi, P. K. Ultra-Sensitive Reusable SERS Sensor for Multiple Hazardous Materials Detection on Single Platform. J. Hazard. Mater. 2021, 407, 124353.

[51]. Wang, C.; Du, J.; Wang, H.; Zou, C.; Jiang, F.; Yang, P.; Du, Y. A Facile Electrochemical Sensor Based on Reduced Graphene Oxide and Au Nanoplates Modified Glassy Carbon Electrode for Simultaneous Detection of Ascorbic Acid, Dopamine and Uric Acid. Sens. Act. B Chem. 2014, 204, 302–309.